CCFE
CULHAM CENTRE FOR FUSION ENERGY

UK Atomic Energy Authority

UKAEA-CCFE-PR(20)72

A. Hollingsworth, M.-F. Barthe, Z. Hu, P. Desgardin, M.Yu. Lavrentiev, S.L. Dudarev, P. Derlet, D. Mason, J. Hess, S. Davies, B. Thomas, H. Salter, E.F.J. Shelton, K. Heinola, K. Mizohata, A. De Backer, A. Baron-Wiechec, I. Jepu, E. Zayachuk, A. Widdowson, E. Meslin, A. Morellec

Deuterium retention and positron annihilation spectroscopy of self-irradiated tungsten

Deuterium retention and positron annihilation spectroscopy of self-irradiated tungsten

A. Hollingsworth, M.-F. Barthe, Z. Hu, P. Desgardin, M.Yu. Lavrentiev, S.L. Dudarev, P. Derlet, D. Mason, J. Hess, S. Davies, B. Thomas, H. Salter, E.F.J. Shelton, K. Heinola, K. Mizohata, A. De Backer, A. Baron-Wiechec, I. Jepu, E. Zayachuk, A. Widdowson, E. Meslin, A. Morellec

This is a preprint of a paper submitted for publication in Journal of Nuclear Materials

Deuterium retention and positron annihilation spectroscopy of self-ion irradiated tungsten

A. Hollingsworth[a*], M.-F. Barthe[b], M.Yu. Lavrentiev[a], P.M. Derlet[c], S.L. Dudarev[a], D. Mason[a], Z. Hu[b], P. Desgardin[b], J. Hess[a], S. Davies[a], B. Thomas[a], H. Salter[a], K. Heinola[d], K. Mizohata[d], A. De Backer[a], A. Baron-Wiechec[a,e,f], I. Jepu[g], Y. Zayachuk[a], A. Widdowson[a], E. Meslin[h], A. Morellec[h]

[a]*UK Atomic Energy Authority, CCFE, Culham Science Centre, Abingdon, Oxon, OX14 3DB, United Kingdom*
[b]*CNRS, CEMHTI UPR3079, Univ. Orléans, F-45071 Orléans, France*
[c]*Condensed Matter Theory Group, Paul Scherrer Institut, CH-5232, Villigen PSI, Switzerland*
[d]*Department of Physics, University of Helsinki, Helsinki, Finland*
[e]*Technion – Israel Institute of Technology, Haifa 32000, Israel*
[f]*Guangdong Technion – Israel Institute of Technology, Shantou 515063, PR China*
[g]*Laboratory of Low Temperature Plasma, National Institute for Laser, Plasma and Radiation Physics, Magurele, Romania*
[h]*DEN-Service de Recherches de Métallurgie Physique, CEA, Université Paris-Saclay, F-91191, Gif-sur-Yvette, France*

Abstract

Self-ion irradiation of pure tungsten with 2 MeV W ions is used for simulating microstructures created by neutron irradiation in a fusion reactor. Electron microscopy was then applied to characterizing the defects formed in the samples as a result of ion irradiation. Some of the irradiated samples were then implanted with deuterium. Thermal Desorption Spectrometry (TDS) was performed to estimate the deuterium inventory as a function of irradiation damage. Application of Positron Annihilation Spectroscopy (PAS) to self-irradiated but not deuterium implanted samples enabled assessing the density of irradiation defects as a function of the exposure to high-energy ions. The PAS results show that the density of defects saturates at doses in the interval from 0.085 and 0.425 displacements per atom (dpa). These results are discussed in the context of recent theoretical simulations exhibiting the saturation of defect microstructure in the high irradiation exposure limit.

[*]Corresponding author. Email: Anthony.Hollingsworth@ukaea.uk

1. Introduction

Tungsten has relatively high thermal conductivity and mechanical strength at high temperature. These properties have favoured its selection as the primary candidate material for the divertor of ITER [1,2], as well as a prospective material for the divertor and first wall components in DEMO [3,4]. It is expected that in ITER and DEMO tungsten will be exposed to extreme conditions, including direct contact with fusion plasma as well as high neutron flux. The challenges associated with the operation of tungsten components include the quantitative characterization and understanding of evolution of mechanical properties as well as tritium retention. Retention of hydrogen and its isotopes are known to alter physical and mechanical properties of materials, and the loss of radioactive inventory is problematic both in terms of resource scarcity and regulatory constraints [5]. Furthermore, exposure to high energy ions and neutrons give rise to displacement cascades and produces defects in the microstructure. This requires investigating the damage that irradiation generates in tungsten, including the production of defects (vacancies and interstitials), their complexes (loops and cavities), and extended dislocation network. One of the significant questions related to the assessment of hydrogen isotope retention is the evaluation of how the density of defects, particularly vacancies, depends on the irradiation dose, since vacancies and vacancy clusters are known to act as traps for hydrogen isotopes and helium [6-8].

In this paper, we describe results of an experimental study, supported by theoretical analysis and simulations, of self-irradiated tungsten performed within the UKAEA led Europe-wide Tritium Retention in Controlled and Evolving Microstructure (TRiCEM) project. Some of the tungsten samples were exposed to deuterium plasma at room temperature in a new facility that enables studying the interaction of hydrogen isotopes with nuclear fusion relevant first wall materials, and retention and release of these isotopes. The new facility enables implanting a range of gases into the samples, these gases include tritium. The design and build of this facility and the commissioning results are described in detail in a recent publication [9]. After implantation, the samples were studied using several experimental techniques, including Thermal Desorption Spectroscopy (TDS) and Transmission Electron Microscopy (TEM). Our aim was to identify peaks in the TDS spectra of irradiated tungsten, to investigate the dependence of deuterium inventory on irradiation damage and to compare the data with earlier experimental results. Next, we performed PAS analysis of the samples, using PAS as an

established technique for the detection of vacancy-type defects [10-12]. PAS is sensitive to small defects from a single vacancy to vacancy clusters and has the detection limit (depending on the material and the nature of the defects) in the range from about 10^{23} m^{-3} down to about 10^{20} m^{-3}, hence enabling a fairly precise determination of the density of defects.

The paper is organized as follows. In Section 2, we describe the preparation of samples used in this study, and their characterization using electron microscopy and TDS. In Section 3, we present the results of PAS analysis and give estimates for the level of damage as a function of irradiation dose. We discuss the results and their relation to recent developments in modelling and simulation of defects in materials Section 4 and conclude in Section 5.

2. Material preparation and characterization

2.1. Preparation

Hot-rolled, 99.95% guaranteed pure sheet sections of tungsten were purchased from Plansee. The material was annealed in a vacuum (6×10^{-6} mbar) furnace for 20 hours at 1500°C. Circular discs of 500 µm thickness were cut from the as-received rods using a Struers cutting saw. The samples were then polished in several stages with abrasive SiC paper form FEPA P250 to P4000 to 100 µm thickness, producing a flat surface with a thin deformation layer. Chemo-mechanical polishing using colloidal silica suspension (0.05 microns) has been used to obtain a mirror surface finish. The polished samples were then cleaned in an ultrasonic bath with iso-propanol for 15 minutes and then acetone for a further 15 minutes. Discs of 3 mm diameter were punched out from the polished specimen. One-side specimens were jet-electropolished in a Tenupol-5 thinning device for a few seconds to obtain mirror finished dimpled discs. The polishing bath was composed of 2 g NaOH in 1 litre of demineralized water following Yi *et al*. [13]. Prepared samples were shipped to the accelerator laboratory at the University of Helsinki where high energy ions were used to damage the microstructure. Irradiation was performed using raster-scanned beam at room temperature. The ion species used for this work are 2 MeV W^+ and the flux was 1.15×10^{15} ion/m^2/s. The dependence of damage (measured in displacements per atom, dpa) as a function of depth from the surface is shown in Figure 1. It was calculated for the total fluence of ~0.7×10^{18} ion/m^2 obtained after irradiation time of 615 s using two methods: the SRIM software [14-16] using the Kinchin-Pease model as suggested in [15] assuming the displacement threshold energy E_d=54 eV. Also, the Binary Collision

Approximation (BCA++) method described in [17,18] was used in order to calculate the total cascade volume fraction. The maximum damage at around 100 nm from the surface is 0.5 dpa.

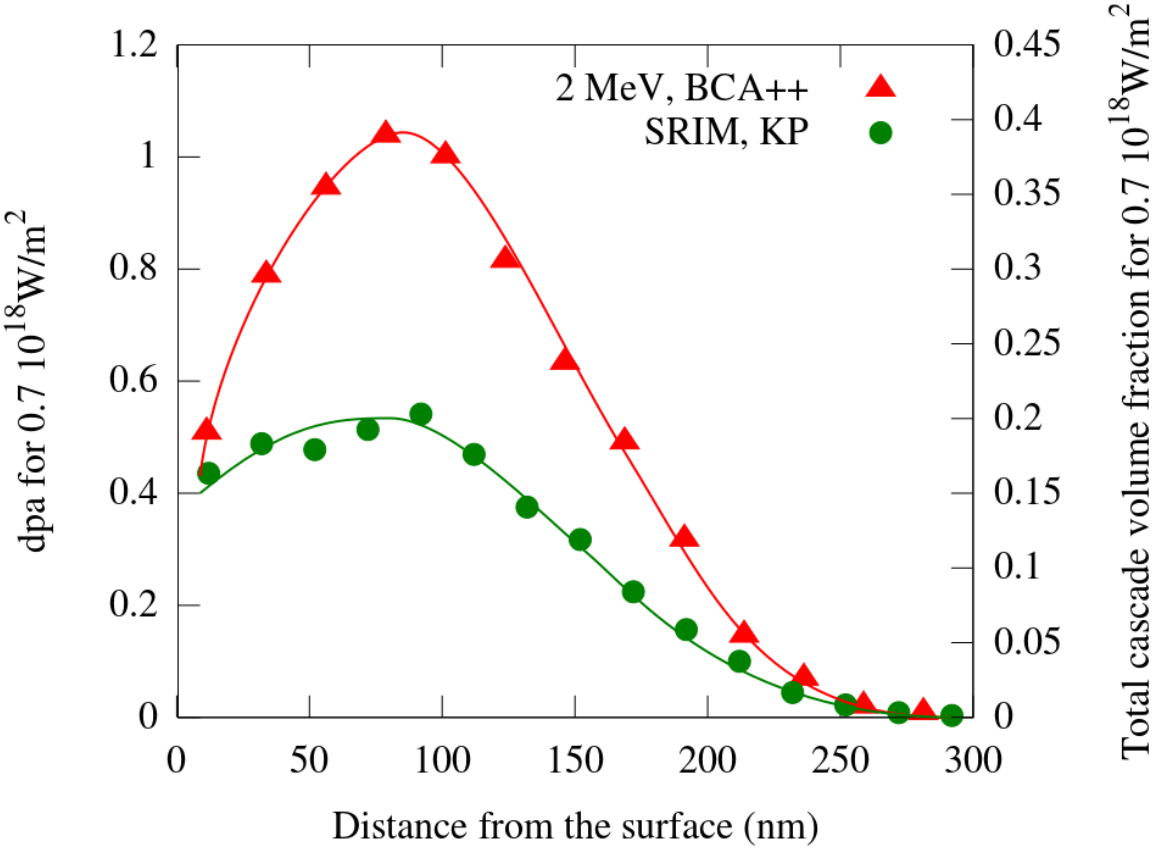

Figure 1. Damage (dpa, left scale) according to SRIM with Kinchin-Pease (KP) option, and the total cascade volume fraction (right scale) as function of depth.

The samples used in this study are summarized in Table 1. Deuterium implanted samples were used for TDS and TEM studies, while unimplanted samples were studied using Positron Annihilation Spectroscopy method.

Sample	Irradiation fluence (2 MeV W^+), atoms/cm^2	Irradiation time (s)	Self-irradiation dose (dpa)	Deuterium implanted?	Characterization
S17	0	0	0	Yes	TDS
S37	0	0	0	Yes	TDS

S40	1×10^{14}	180	0.85	Yes	TDS
S41	1.2×10^{13}	19	0.085	Yes	TDS
S42	1.8×10^{12}	3	0.0085	Yes	TDS
S112	0	0	0	No	PAS
S113	1×10^{12}	53	0.0085	No	PAS
S116	1×10^{13}	477	0.085	No	PAS
S119	5×10^{13}	2289	0.425	No	PAS
S123	1×10^{14}	4424	0.85	No	PAS
S125	2×10^{14}	8406	1.7	No	PAS

Table 1. List of the samples used in the current study.

2.2. Electron Microscopy

A conventional FEI 20 G2 Tecnai Transmission Electron Microscope, located at CEA Saclay and equipped with a LaB_6 source delivering 200 keV electrons, was used. Bright Field (BF) and Weak Beam Dark Field (WBDF) images were recorded to study irradiation features such as dislocation loops and lines. A camera Gatan Orius 200D has been used to record images and movies. The latter were recorded at a rate of 30 images per second.

Before irradiation, the material presented a typical annealed structure, composed of micrometric grains and a low density of dislocation lines (~$10^{12}/m^2$) (Figure 2). The mean grain size as determined by scanning electron microscopy (SEM) is about 90 µm.

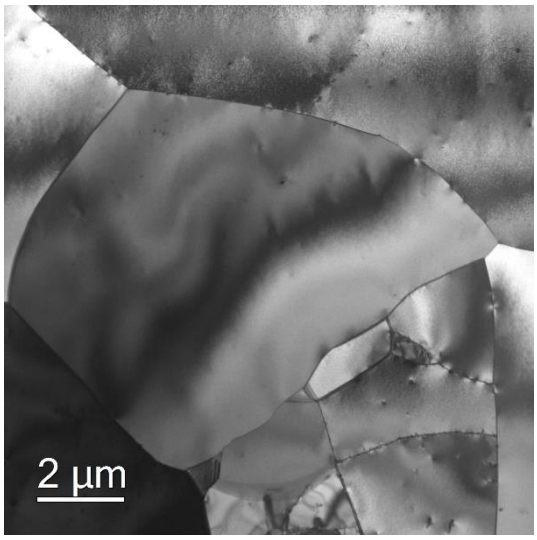

Figure 2. Low magnification TEM image of the electropolished tungsten before irradiation (BF image).

After irradiation, formation of a high density of irradiation defects was detected (Figure 3). They are in the form of dislocation loops and black dots. The same method as in [19] was used for determining their size distribution, shown in the Figure 4. In total, 1279 objects were included in the measurements. The mean size and the density of defects per surface unit area of the sample were found to be 3.4±0.1 nm and $(3.94\pm0.1)\times10^{13}$ loops/m², respectively. The statistical error of measurements is also shown.

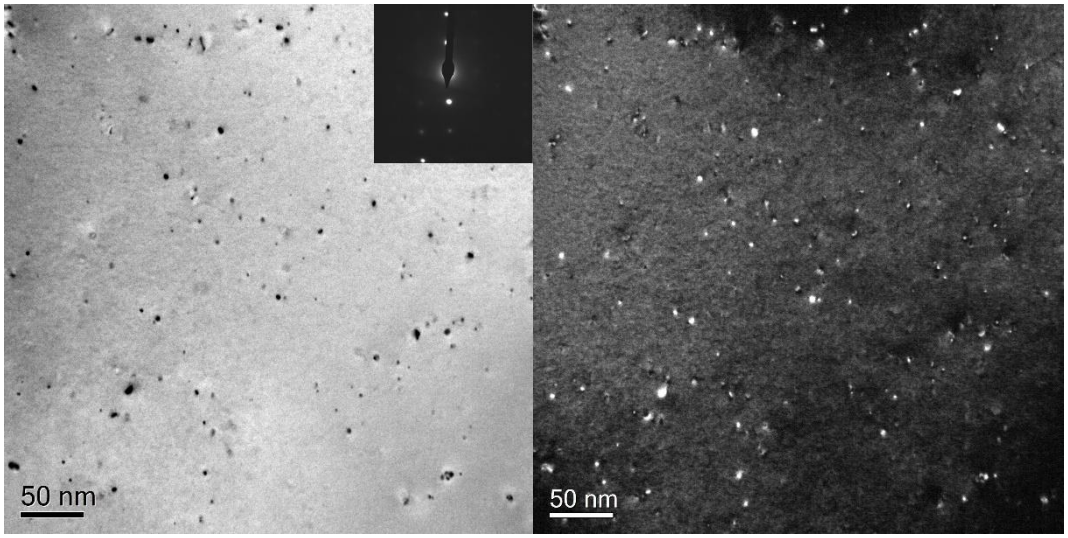

Figure 3. Bright field (left) and weak beam dark field images (right) of tungsten irradiated up to 0.85 dpa at peak at room temperature. Images were taken along a <001> zone axis using a **g**=<011> type diffraction vector.

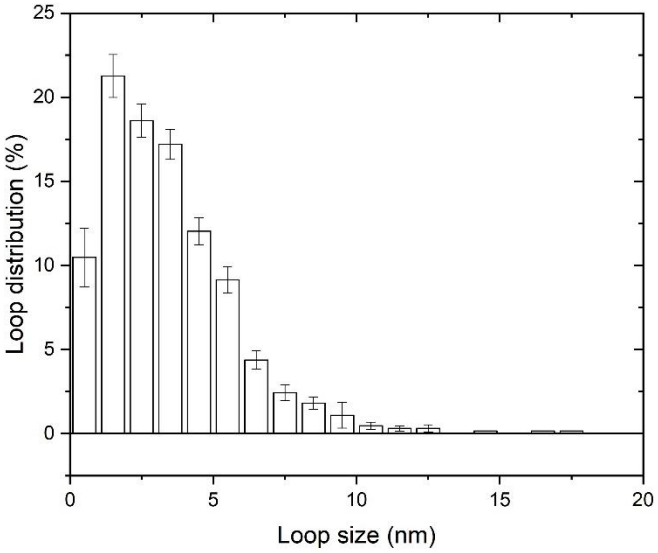

Figure 4. Size distribution of loops formed in tungsten irradiated up to 0.85 dpa at peak dose at room temperature. Bright field electron microscope images were used to determine this distribution.

An electron beam induced defect mobility has been noted during the observation with 200 keV electrons at room temperature. Examples of loop jumps are given in Figure 5. Similar mobility was reported recently [20].

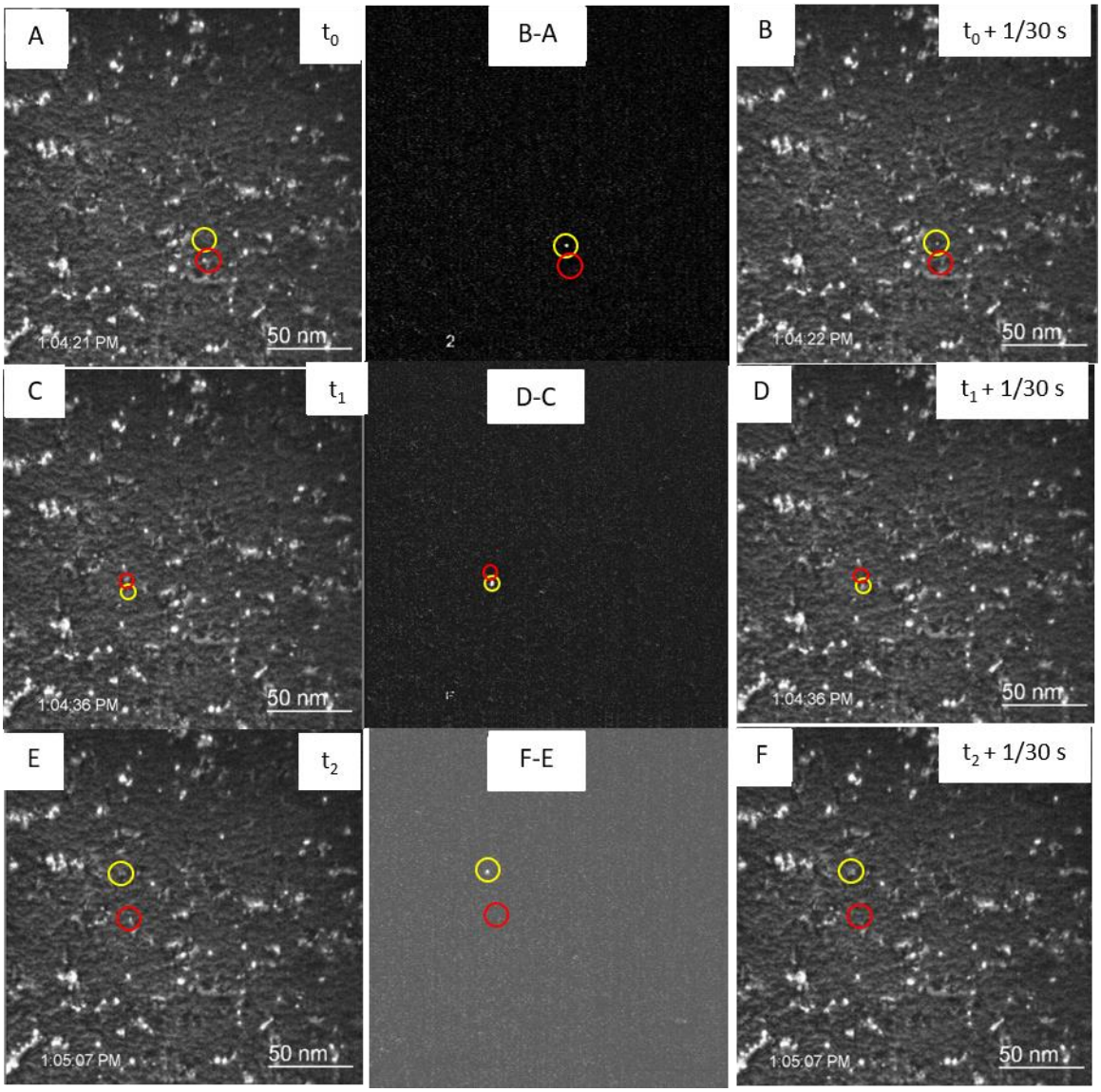

Figure 5. Three series of images extracted from the observation using 200 keV electron beam in tungsten irradiated up to 0.85 dpa at peak at room temperature (WBDF image, **z**=<001>, **g**=<110>). An image subtraction is shown in the middle to highlight the loop jump between A and B, C and D, and E and F frames. The initial position of the defect is highlighted by red circles, while the final position of the loop is highlighted by yellow circles.

2.3. Thermal Desorption Spectrometry

After exposure to deuterium plasma up to an estimated fluence of 10^{23} D/m^2 (plasma temperature 50 °C, ion energy 400 eV), TDS of deuterium implanted samples was performed at a constant rate of 10 K/min between room temperature and 1000°C. The resulting spectra are shown in Figure 6. The spectra for all the irradiated samples (S40-S42) and one unirradiated sample (S17) are characterized by a wide maximum between 350-400 K and 550-600 K. This maximum has been detected previously in the case of low-temperature implantation [21] and it was suggested that it might be attributed to release of deuterium from several possible traps, such as grain boundaries or surface adsorption sites. Also, vacancies with multiple population might contribute to desorption in this temperature range for irradiated samples, as it was shown that with increasing population of traps, binding energy of hydrogen isotopes decreases [7,8]. Absence of this low-temperature peak in unirradiated sample S37 can be related to a long delay between implantation and the TDS measurements, allowing surface deuterium to leave. This low-temperature peak is also absent in experimental studies in which deuterium implantation was performed at elevated temperatures: 470 K [22]. Recent study in which tungsten samples were initially simultaneously self-irradiated and exposed to 300 eV deuterium ions at temperatures between 450 K and 1000 K with subsequent additional exposure at 450 K [23] also produced TDS peaks around 600 K. Second large peak is more narrow and centered around 700-750 K, in agreement with other results [21-23]. Usually this peak is attributed to deuterium release from single vacancies. Finally, wide small peak was detected at around 1100 K in all irradiated samples. This peak has not been observed in previous studies, in which TDS spectra were usually obtained up to no more than 1000 K. The height of all peaks in irradiated samples increased with increasing irradiation dose.

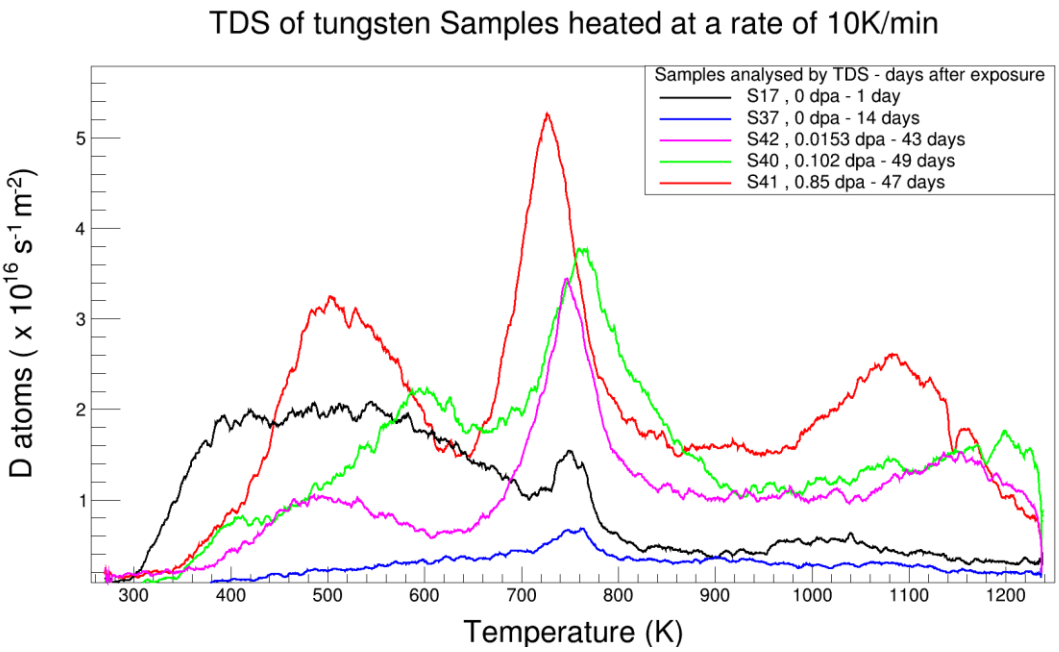

Figure 6. TDS spectra of implanted samples with damage levels between 0 and 0.85 dpa. Time period between exposure to deuterium plasma and the TDS is shown in the inset.

3. PAS Analysis

3.1. Description of the PAS system and method used

The samples were characterized by using a slow positron beam coupled to a Doppler broadening spectrometer (SPB-DB) available at the CEMHTI laboratory. A comprehensive description of the experimental setup and the basics of this powerful method are described in [24]. A monoenergetic positron beam, with a diameter of 3 mm, was generated from a ^{22}Na source. The positron beam energy was varied in the range of 0.5 to 25 keV. The spectrum of the γ-ray annihilation photons (centered at 511 keV) coming from the sample is recorded using a high-resolution gamma spectrometer equipped with a germanium detector (1.24 keV resolution at 514 keV). This Doppler broadened spectrum is characterized by two line-shape parameters: *S* and *W*. *S*, defined as the ratio of counts in the central region of the spectrum to the total counts, represents the fraction of positron-electron pairs annihilated with low momentum and is thus related mostly to annihilations with valence electrons. *W*, the ratio of counts in the wing regions of the spectrum to the total counts, represents the fraction of positron-electron pairs annihilated with high momentum and hence is more specifically related to the annihilations of positrons with core electrons. For our experiments, the momentum ranges for the calculation of *S* and *W* are 0- $|2.80| \times 10^{-3}\ m_e c$ and $|10.61| \times 10^{-3}$ - $|26.35| \times 10^{-3}\ m_e c$, respectively, where m_e is electron mass and c the speed of light. These momentum ranges correspond to ranges of energies of annihilation emitted photons being 510.28 – 511.72 keV

for the *S* photons and 504.27 – 508.29 keV and 513.71 – 517.73 keV for the *W* photons. Each material exhibits specific S_L and W_L values, the signature of the momentum electrons distribution in the perfect lattice in the absence of vacancy defects. The sensitivity of the PAS technique to the type and concentration of vacancy defects in solids resides in the fact that positrons are more susceptible to being trapped in these defects, where the electron density is low, before annihilating. When positrons are trapped at vacancies, their smaller overlap with core electrons narrows the positron-electron momentum distribution resulting in an increase of *S* and a decrease of *W*. Hence *S* and *W* yield information about the presence of vacancy defects in solids and *S* increases and *W* decreases. To each type of vacancy clusters *j* correspond specific values of S_j and W_j. Generally, *S* increases and *W* decreases when the number of vacancies *N* in the cluster V_N increases. Moreover, it has been demonstrated that the $\left|(S_{VN}-S_L)/(W_{VN}-W_L)\right|$ ratio also increases with increasing *N* [25]. *S* and *W* values are related to the positron trapping rate K_d at the detected defects, which is the product of their concentration C_d and their specific trapping coefficient μ_d. The trapping coefficient of single vacancy is approximated to the value determined for the single vacancy in Ta which presents the closest *Z* value ($\mu_V = 6 \pm 3 \times 10^{-9}$ cm^3/s [10]). It is expected that the specific trapping coefficient for vacancy clusters V_N is *N* times the one of the single vacancy ($\mu_{VN} = N \times \mu_V$).

Note that positrons can be also trapped in <100> edge and ½ <111> screw dislocations as it has been calculated in iron and tungsten [26] and observed in iron [27] and in tungsten [28]. The specific annihilation characteristics S_j, W_j of this type of defects have not yet been determined in tungsten. Only calculations of the positron lifetime can be found in the literature [26,29]. Depending on the nature of the dislocation, the lifetime changes generally between a value close to the lifetime in the perfect lattice (τ_L =101 ps in tungsten [30] and the one in the single vacancy (τ_V =193 ps in tungsten) [26] due to the fact that open volume is lower in the core of a dislocation than in a vacancy. The lifetime in ½ <111> screw and <100> edge dislocations has been calculated to be 130 ps and 161 ps, respectively [26]. When vacancies are bound to the dislocation line the lifetime increases and reaches a value close to the lifetime of the bounded vacancy cluster. The same conclusions have been found for iron [26]. Recently the S_{dis}, and W_{dis} specific to dislocations have been detected in iron [31]. As expected, the characteristic $\left|(S_{dis}-S_L)/(W_{dis}-W_L)\right|$ ratio is lower than the one for the single vacancy V $\left|(S_V-S_L)/(W_V-W_L)\right|$. The same relationship is also expected for the bcc tungsten. The trapping coefficient of positrons at the dislocation μ_{disl} is not known for tungsten.

For this study, *S(E)* and *W(E)* were recorded as functions of positron energy ***E*** spanning the range from 0.5 to 25 keV. This energy range corresponds to the mean positron implantation depth in tungsten between approximately 0.4 and 300 nm. Note that the full-width-at-half-maximum of the implanted positrons distribution increases with the energy, to reach ≈ 380 nm at 25 keV. At this energy, positrons probe up to ≈ 700 nm under the tungsten surface, i.e. all of the damaged region, as can be seen in Figure 7. The *S* value measured at the energy *E* depends on the defects distribution and diffusion properties of the positrons in the sample. A modified version of VEPFIT program [32] allows the calculation of *S(E)* and *W(E)* taking into account the positrons implantation and their diffusion considering the defect depth profile is a sequence of homogeneous layers. Note that the diffusion of positrons is limited by their trapping in defects and the effective diffusion length that L_{eff}^{+} can be written as follows [33]:

$$L_{eff}^{+} = \sqrt{\frac{D^{+}}{\lambda_L + \sum_1^n K_{d_i}}}$$

where K_{di} are the positron trapping rates at the various detected defects (single vacancy, vacancy clusters V_N, dislocations etc.), D^+ is the intrinsic positron diffusion coefficient (D^+ = 1.26×10^{-4} m^2/s for tungsten [34]), and λ_L the lattice annihilation rate ($\lambda_L = 1/\tau_L$, τ_L= 101-105 ps [30,35]). Hereafter, VEPFIT is used to consistently fit the *S(E)* and *W(E)* curves allowing to extract the *S(z)* and *W(z)* depth profiles and the effective diffusion length in each layer. Note that the data for the positron energy below 2.0 keV were discarded because for this low energy, the positrons migration does not result, in the present case, in a diffusion process.

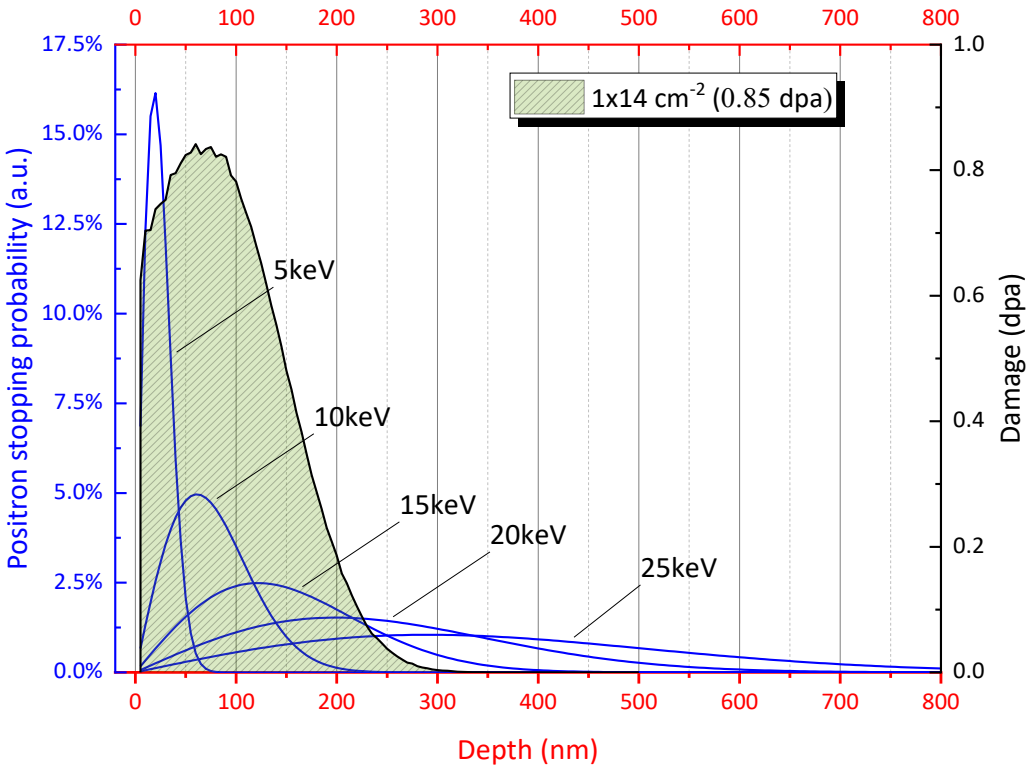

Figure 7. The implantation profiles of 5, 10, 15, 20 and 25 keV positrons in tungsten compared to the SRIM calculations of the damage profile of 2 MeV W^+ ions implanted at a 1×10^{14} atoms/cm^2 fluence at room temperature, taking a displacement threshold energy of 55 eV [36,37] in the Kinchin-Pease model as recommended by Stoller *et al.* [15].

Line-shape parameter $S(z)$ (or in the case where the vacancy defect depth profile is modelled as a succession of homogeneous layers, $S_{lay}(i)$ corresponding to the S value in layer i) is related to the specific values S_j of trapping defects j at which positrons are annihilating and the fraction of annihilation of these defects f_j (related to their concentration). Also, $W(z)$ (or $W_{lay}(i)$) can be expressed in the same way:

$$S_{lay}(i) = \sum_{j=1}^{n} S_j \times f_j, \qquad W_{lay}(i) = \sum_{j=1}^{n} W_j \times f_j$$

Some annihilation characteristics have been already experimentally determined in tungsten. For the perfect lattice, the annihilation characteristics are $S_L = 0.367(4)$ and $W_L = 0.084(5)$; for the single vacancy, $S_V = 0.417(1)$ and $W_V = 0.057(1)$ [38,39]. The maximum and minimum values of line-shape parameters were obtained from previous studies we carried out in tungsten and are as follows: $S_{Max} = 0.5026$, $W_{Min} = 0.03636$. They correspond to the detection of large vacancy clusters V_N. Note that the specific values of S_{VN} and W_{VN} for positron annihilation as trapped in the different types of vacancy clusters are not known. But the maximum and minimum values S_{Max} and W_{Min} are most probably related to the annihilation in vacancy clusters with the maximum size detectable with SPB-DB.

The *S(E)* and *W(E)* curves measured in unirradiated tungsten sample are plotted in Figure 8. These experimental data can be fitted with the VEPFIT program, considering the sample as one homogeneous layer. The line-shape parameters for unirradiated sample are S_{unirr} = 0.370(1), W_{unirr} = 0.083(1). These values are respectively slightly higher and lower than the perfect lattice parameters S_L and W_L. This indicates that some of the positrons annihilate while trapped in vacancy defects, but the concentration of these defects remains low. This is also confirmed by the high value of the effective diffusion length of 80±1 nm which appears to be very close to the values available in literature for perfect crystalline tungsten [33,38], namely 80–135 nm. This indicates that the concentration of defects in the bulk of un-irradiated sample is low, and lower than 10^{24} m^{-3}.

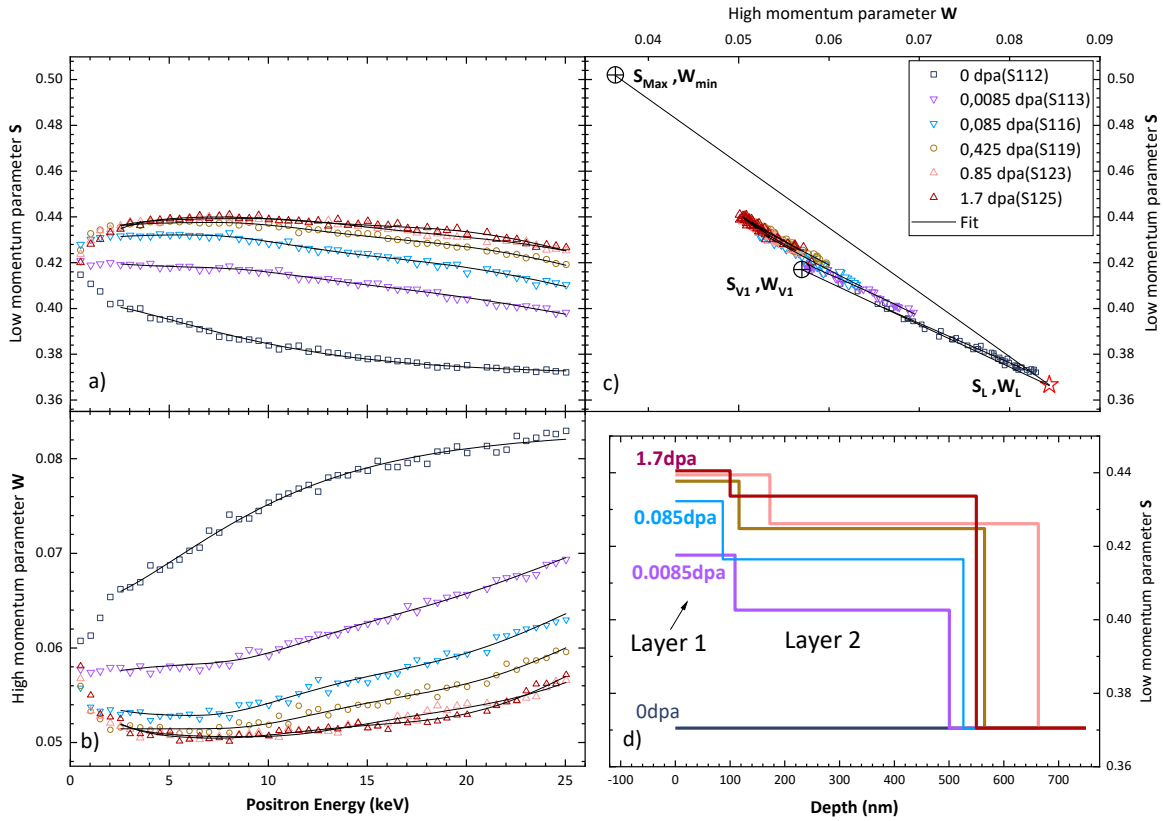

Figure 8. Evolution of the positron annihilation characteristics in unirradiated tungsten sample and in samples after irradiations at damage doses between 0.0085 and 1.7 dpa. (a) Low momentum fraction *S*, and (b) high momentum fraction *W* as functions of the positron energy. (c) *W* plotted as a function of *S*. The *S*, *W* values for the annihilation in lattice (S_L, W_L), single vacancy (S_{V1}, W_{V1}), and maximum *S* and minimum *W* are also plotted (S_{Max}, W_{Max}). The experimental data are plotted in open symbols and the fitted curves are given in continuous line. (d) the *S(z)* and *W(z)* depth profiles extracted from *S(E)* and *W(E)* using VEPFIT (see details in the text).

3.2. As-irradiated results

Line-shape parameters *S(E)* and *W(E)* measured after irradiation with 2 MeV tungsten ions at various fluences are plotted in Figure 8. With increasing irradiation dose, the *S* and *W* values drastically increase and decrease, respectively. This indicates that positrons respond to the presence of defects generated during implantation for all the fluences studied.

For the sample irradiated at the lowest dpa level (0.0085 dpa), *S* remains constant in the energy range between 0.5 and 8 keV and then decreases slowly. This indicates that the damage level decreases when depth increases, as has been calculated using SRIM. The $|(S\text{-}S_L)/(W\text{-}W_L)|$ ratio for the plateau values (1.96(4)) is higher than the one for the single vacancy (1.85(3)) indicating that vacancy clusters are also detected. These clusters are probably formed in the collision cascades. Fitting of the *S(E)* and *W(E)* with the VEPFIT program requires a model with a minimum of 3 homogeneous layers to describe correctly the experimental curves. Models with 3 and 4 layers has been tested. The one with 3 layers has been chosen because the number of parameters to be fixed is minimised, and the quality of the fit is acceptable. In these fits the annihilation characteristics of the last layer, which is not damaged, have been fixed at the values $S_{Lay}(3)$ = 0.370, $W_{Lay}(3)$ = 0.083 and the effective diffusion length $L_{Lay}(3)$ was taken to be 80 nm in agreement with the values obtained in the bulk of the unirradiated samples. The annihilation characteristics extracted for layers 1 and 2, S_{Lay}, W_{Lay}, and L_{Lay} are reported in the Table 2. The thickness of the first layer is about 100 nm for all the irradiated samples, a value close to the depth of maximal damage at the maximum dpa level calculated using SRIM. The $S_{Lay}(1)$, $W_{Lay}(1)$ values extracted from the fitting correspond to the maximum damage induced for each damage dose. Note that these values represent the mean of *S(E)* and *W(E)* calculated in the energy range between 7 and 8.5 keV.

Damage dose (dpa)	Layer 1					Layer 2			
	S_{Lay}	W_{Lay}	$(S_{Lay}\_S_L)/(W_{Lay}\text{-}W_L)$	L_{Lay} (nm)	Thickness (nm)	S_{Lay}	W_{Lay}	L_{Lay} (nm) fixed	Thickness (nm)
0.0085	0.418(1)	0.058(1)	1.96(4)	14(4)	100(10)	0.402(2)	0.067(2)	60	510(10)
0.085	0.432(1)	0.053(1)	2.10(4)	2-6	93(6)	0.417(2)	0.059(2)	50	510(20)
0.425	0.438(1)	0.051(1)	2.15(4)	2-6	105(10)	0.425(3)	0.057(1)	40	570(10)
0.85	0.440(1)	0.050(1)	2.15(4)	2-6	100-170	0.428(5)	0.054(2)	30	610(65)
1.7	0.440(1)	0.050(1)	2.15(4)	2-6	100-170	0.428(7)	0.054(4)	30	610(65)

Table 2. Annihilation characteristics $S_{Lay}(i)$, $W_{Lay}(i)$, and $L_{Lay}(i)$ for the layers i = 1,2, extracted from the fitting of the *S(E)* and *W(E)* with the VEPFIT program using a three layers model for irradiated samples at different damage doses between 0.0085 and 1.7 dpa.

$S_{Lay}(1)$ increases and $W_{Lay}(1)$ decreases first rapidly when damage dose increases up to 0.085 dpa and more slowly up to 0.85 dpa. They remain constant when damage dose is increased by

a factor of 2. The saturation values of $S_{Lay}(1)$ and $W_{Lay}(1)$ are $S_{Sat}(1)$ = 0.440(1) and $W_{Sat}(1)$ = 0.050(1). Note that they are the same as the values obtained for damage of 1 dpa and also at 12 dpa using other irradiation conditions (20 MeV W^+ ions at room temperature [40]).

The $\left|(S_{Lay}(1)-S_L)/(W_{Lay}(1)-W_L)\right|$ ratio also increases slightly when damage dose increases up to 0.425 dpa indicating that the proportion of the largest vacancy clusters increases probably due to the overlapping of collision cascades. Overall, PAS results detect a saturation of damage when the dpa level becomes higher than 0.425 dpa. The $S_{Lay}(1)/S_L$ normalised values measured in the irradiated samples are plotted as a function of dpa level in Figure 9.

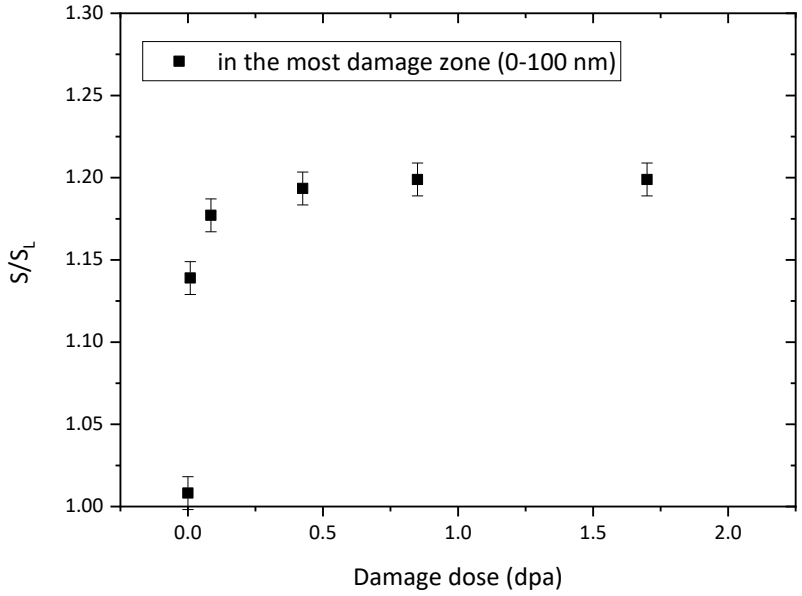

Figure 9. Low momentum annihilation fraction in the most damaged zone as a function of dpa level in self irradiated (2 MeV W^+ ions) tungsten samples.

4. Discussion

We have seen above that the *S* and *W* values obtained in the most damaged zone of self-irradiated tungsten samples vary with damage dose. The *S, W* values in the sample irradiated at the lowest damage dose (0.0085 dpa) are very close to the annihilation characteristics of single vacancy suggesting that they are the major defects. The concentration of these vacancies C_V can be estimated from the effective diffusion length using a one trap trapping model where positron can annihilate in only one type of defects the single vacancy. C_V can be written as follows:

$$C_V = {}^{\lambda_L}/_{\mu_V}\left[\left({}^{L^+}/_{L_{eff}^+}\right)^2 - 1\right]$$

where L_{eff}^+ is the effective diffusion length in the damaged layer, L^+ is the intrinsic positron diffusion length (80-135 nm), λ_L the lattice annihilation rate ($\lambda_L = 1/\tau_L$), and μ_V the trapping coefficient at the single vacancy.

For the lowest damage dose, L_{eff}^+ has been found to be equal to 14(4) nm (see Table 2) and the corresponding vacancy concentration reaches the mean value of 9.2×10^{25} m^{-3}. As the damage dose increases, we observe that L_{eff}^+ decreases, indicating that trapping of positrons increases and that vacancy clusters are detected. The one trap trapping model can no longer be used and *S* and *W* values become the results of annihilation of positrons as trapped in vacancy defects single vacancy and vacancy clusters and possibly at some dislocation type defects. TEM results presented in Section 2.2 showed that dislocation loops are generated in self-irradiated sample as it has been already observed in literature (see [41], for example). Their density per unit area is estimated to be $(3.94\pm0.1)\times10^{13}$ loops/m^2, at 0.85 dpa. If we consider that the thickness of the sample is in the range from 50 to 150 nm (to ensure that the sample is transparent to 200 keV electrons) the volume density can be estimated to be in the range from $3\text{-}8\times10^{20}$ m^{-3}. We note that this density was evaluated using only one diffraction vector **g** =<110>. If we assume that both families of <100> and ½ <111> loops are generated in the same proportion during irradiation, we estimate from the invisibility rules that only 60% of the dislocation loops have been detected. As showed in [41], the fraction of <100> is expected to be lower than the ones of ½<111>. If we consider at the worst case that no <100> loops are created, only 50% of loops are detected in the observation conditions used for this study. Even if we take into account that not all the dislocation loops are detected, their concentration remains low and could be twice the one measured in the TEM micrographs that means should range from $0.6\text{-}1.6\times10^{21}$ m^{-3} for 0.85 dpa. At this damage dose the fraction of positrons that could be trapped at dislocation loops is negligible and positron annihilation characteristics are only representative of vacancy defects trapping including single vacancy and vacancy clusters V_N.

The annihilation characteristics S_{VN}, W_{VN} of vacancy clusters are not known, only some V_N lifetimes (τ_{VN}) have been already calculated [30]. τ_{VN} increases with *N* that means with the size of vacancy clusters and becomes constant when *N* is so high that positron annihilates close to the surface of the cluster, the electron density being negligible in the vacancy cluster. This

saturation occurs when N becomes larger than 20 vacancies [30]. S_{max} and W_{min} correspond to this saturation in tungsten and, by this way, to positrons annihilation in the largest vacancy clusters V_N for which the size can no more be distinguished in PAS. The $\left|(S_{max}-S_L)/(W_{min}-W_L)\right|$ ratio (equal to 2.8) can be assigned to annihilation in vacancy cluster V_N where N is larger than 20 vacancies. The values of the $\left|(S_{Lay}(1)-S_L)/(W_{Lay}(1)-W_L)\right|$ ratio, in the damaged layer, reach 2.15 at the maximum, which correspond to an intermediate value between the V_N related ratio ($\left|(S_{max}-S_L)/(W_{min}-W_L)\right|$ =2.8) and the single vacancy one ($\left|(S_V-S_L)/(W_V-W_L)\right|$ = 1.8). It suggests that the vacancy clusters V_N detected in the damaged layer are small and N is probably not larger than 5-7. So when damage dose becomes larger the lowest value 0.0085 dpa, positrons annihilate as trapped in single vacancy and in V_N with N varies from 2 to 5-7.

The concentration of each type of defects cannot be determined because not only the S_{Vi}, W_{Vi} of vacancy clusters are not known but also their corresponding annihilation fractions cannot be extracted. It is therefore possible to extract from the effective diffusion length L_{eff}^{+} obtained in the damaged layer the total vacancy defects concentration. Indeed, L_{eff}^{+} can be written as follows

$$L_{eff}^{+} = \sqrt{\frac{D_+}{\lambda_L + K_V + \sum_2^{5-7} K_{V_N}}}$$

Where K_V and K_{VN} are the positron trapping rates at the single vacancy and the vacancy clusters V_N respectively. For L_{eff}^{+} = 4 nm (see table 2), $K_V + \sum_2^{5-7} K_{V_n}$ = 7.2×10^{12} s^{-1}. K_V is the product of the trapping coefficient μ_V by the vacancy concentration C_V and $K_{V_n} = \mu_{V_n} \times C_{V_n}$ and $\mu_{V_n} = n \times \mu_V$. It follows that the total vacancy defects concentration C_V^{tot} which is the sum of the isolated vacancy concentration and of the vacancy in vacancy clusters can be estimated from the equation $C_V^{tot} = C_V + \sum_2^{5-7} nC_{V_n} = \frac{(K_V + \sum_2^{5-7} K_{V_n})}{\mu_V}$. In the sample irradiated at the damage dose of 0.085 dpa C_V^{tot} can be estimated at the mean value of 1.1×10^{27} m^{-3} which represents 1.8% of the atomic density of tungsten.

It follows that the total concentration of vacancy defects is 9.2×10^{25} for the lowest damage dose of 0.0085 dpa and increases rapidly to 1.1×10^{27} m^{-3} for 0.085 dpa. When the damage dose becomes higher than 0.085 the total vacancy defects concentration does not change. However, S/S_L slightly increases between 0.085 and 0.425 (Figure 9). It is due to the change of the fraction of the various clusters with the damage dose and more specifically to the increase of the

proportion of the largest clusters which reaches a maximum for 0.425 dpa and becomes constant for higher damage dose.

A similar trend, indicating that the vacancy content in crystalline tungsten exposed to irradiation is expected to increase as a function of dose and reach saturation at a dose above approximately 0.5 dpa, was also found in direct atomistic simulations of highly irradiated tungsten and iron performed using the creation-relaxation algorithm [42]. This algorithm assumes uniform spatial probability distribution of generation of defects, where at each step of execution of the algorithm, a randomly chosen atom is displaced to anywhere within the simulation cell. Upon creation of a Frenkel pair, conjugate gradient minimization of the resulting atomic structure is employed to relax the position of all the atoms towards a local potential energy minimum. The subsequent events of creation and relaxation of defect structures gradually generate microstructure that remains self-similar, showing no further increase of defect content as a function of dose. The dose itself, expressed in terms of the c-dpa parameter, is defined as the ratio of the total number of Frenkel pairs created since the start of the simulation, divided by the total number of atoms in the simulation cell.

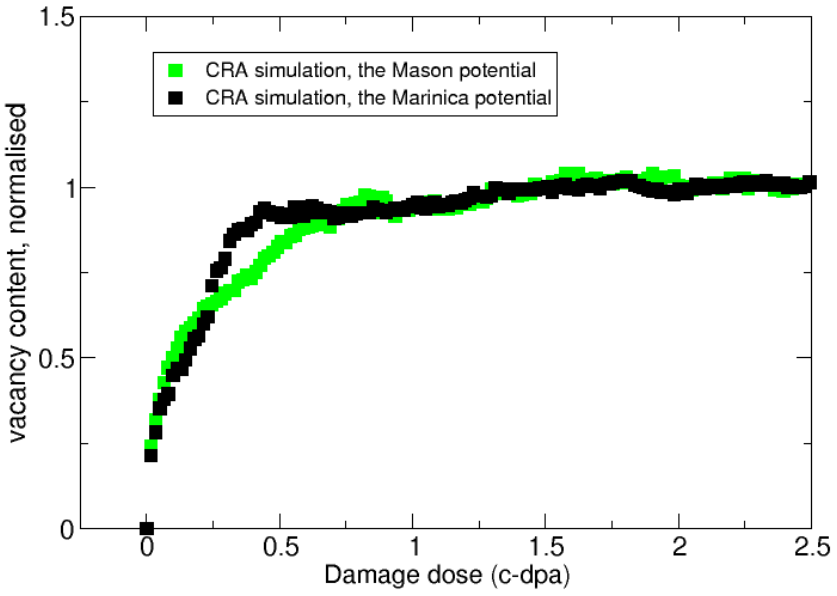

Figure 10. Variation of vacancy content in tungsten as a function of canonical dpa (c-dpa) predicted by simulations performed using the creation-relaxation algorithm (CRA) for two different interatomic potentials [42]. The values are normalised to the asymptotic vacancy content, which for the Marinica potential [43] is close to 5% and for the Mason potential [Mason44] is close to 2%.

The simulations, illustrated in Figure 10, show that after a brief period of linear accumulation that ends at ~ 0.02dpa, vacancy content gradually saturates due to the build-up of internal spatially fluctuating microscopic stress caused by the defects. Similarly to the experimental curve shown in Figure 9, saturation occurs at the dose close to 0.5 dpa. Simulations also show that the density of dislocation loops in the limit of high dose is relatively low, since the majority of self-interstitial defects are incorporated into an extended dislocation network and hence become effectively undetectable by transmission electron microscopy in the form of isolated individual dislocation loops.

Since the algorithm developed in [42] takes into account only the relaxation events driven by local stress and not by thermal fluctuations, it is expected that the absolute vacancy content might be somewhat overestimated. However, given that in irradiated tungsten, vacancies do not diffuse appreciably below 350 °C [45,46], the assumption that thermal relaxation of defect structure is impeded and effectively does not occur at room temperature, is broadly justified and agrees with direct real-space electron microscope observations of thermal annealing of extended dislocation microstructure of heavily irradiated tungsten, which occur only at temperatures close to 800 °C [47].

5. Conclusions

This above study shows that tungsten irradiated to high dose at relatively low temperatures close to room temperature, and below approximately 350 °C, develops a characteristic microstructure dominated by vacancy type defects. The density of self-interstitial dislocation loops is relatively low, in agreement with recent simulations [42] suggesting that self-interstitial defects tend to incorporate themselves into an extended dislocation network that rapidly forms above doses exceeding 0.1 dpa. At the same time, isolated vacancy defects, according to predictions derived from simulations, dominate the microstructure. This agrees with experimental PAS data described above. Implications of the above for the retention of hydrogen isotopes in irradiated tungsten and other materials are significant, and will be assessed in a separate study.

Acknowledgments

Some of the research used equipment at the UKAEA's Materials Research Facility (MRF) which is part of the UK's Henry Royce Institute and National Nuclear User Facility initiatives. We thank the MRF staff for their support. This work was supported by EUROfusion Enabling Research project TRiCEM, Tritium Retention in Controlled and Evolving Microstructure. This work has been carried out within the framework of the EUROfusion Consortium and has received funding from the Euratom research and training programme 2014-2018 and 2019-2020 under Grant Agreement No. 633053. The views and opinions expressed herein do not necessarily reflect those of the European Commission. We acknowledge funding by the RCUK Energy Programme (Grant No. EP/T012250/1). The views and opinions expressed herein do not necessarily reflect those of the European Commission.

References

[1] M. Rieth *et al*., Advances in Science and Technology **73**, 11 (2010).
[2] T. Hirai *et al*., Nuclear Materials and Energy **9**, 216 (2016).
[3] M. Rieth *et al*., Journal of Nuclear Materials **432**, 482 (2013).
[4] D.T. Blagoeva *et al*., Journal of Nuclear Materials **442**, S198 (2013).
[5] B. Lipschultz *et al.*, Massachusetts Institute of Technology Report PSFC/RR-10-4, 2010.
[6] J. Marian *et al*., Nuclear Fusion **57**, 092008 (2017).
[7] K. Heinola *et al*., Phys. Rev. B **82**, 094102 (2010).
[8] K. Ohsawa *et al*., Journal of Nuclear Materials **527**, 151825 (2019).
[9] A. Hollingsworth *et al.*, Nuclear Fusion **60**, 016024 (2020).
[10] P. Hautojärvi and C. Corbel, in: Positron Spectroscopy of Solids: Proceedings of the International School of Physics 'Enrico Fermi', A. Dupasquier and A.P. Mills Jr., (Eds.), IOS Press, Amsterdam, 1995, p. 491.
[11] A. Dupasquier and G. Ottaviani, in: Positron Spectroscopy of Solids: Proceedings of the International School of Physics 'Enrico Fermi', A. Dupasquier and A.P. Mills Jr., (Eds.), IOS Press, Amsterdam, 1995, p. 581.
[12] M.-F. Barthe, "Positron Annihilation Spectroscopy to Characterize Irradiation Induced Vacancy Type Defects in Materials for Nuclear Fission and Fusion", http://www.materials.cea.fr/MINOS2015/MINOS2015_Barthe.pdf.
[13] X. Yi *et al*., Europhys. Lett. **110**, 36001 (2015).
[14] J.F. Ziegler, M.D. Ziegler, and J.P. Biersack, Nuclear Instruments and Methods in Physics Research B **268**, 1818 (2010).
[15] R.E. Stoller *et al*., Nuclear Instruments and Methods in Physics Research B **310**, 75 (2013).
[16] http://www.SRIM.org
[17] A. De Backer *et al.*, Europhys. Lett. **115**, 26001, (2016).
[18] A. De Backer *et al.*, J. Phys.: Condens. Matter **30**, 405701 (2018).
[19] D.R. Mason *et al*., Acta Materialia **144**, 905 (2018).
[20] K. Arakawa *et al*., Nature Materials (2020), https://doi.org/10.1038/s41563-019-0584-0

[21] M. Zibrov *et al.*, Journal of Nuclear Materials **477**, 292 (2016).
[22] O.V. Ogorodnikova, J. Appl. Phys. **118**, 074902 (2015).
[23] S. Markelj *et al.*, Nucl. Fusion **59**, 086050 (2019).
[24] P. Desgardin *et al.*, Mater. Sci. Forum **363-365**, 523 (2001).
[25] M. Hakala, M.J. Puska, and R.M. Nieminen, Phys. Rev. B **57**, 7621 (1998).
[26] P. Staikov and N. Djourelov, Physica B: Condensed Matter **413**, 59 (2013).
[27] Y.-K. Park *et al.*, Phys. Rev. B **34**, 823 (1986).
[28] T.E.M. Staab *et al.*, J. Phys.: Condens. Matter **11**, 1787 (1999).
[29] E. Kuramoto *et al.*, Computational Materials Science **14**, 28 (1999).
[30] T. Troev *et al.*, Nuclear Instruments and Methods in Physics Research B **267**, 535 (2009).
[31] W. Asplet, "Experimental study of the interaction of vacancy defects with Y, O and Ti solutes to better understand their roles in the nanoparticles formation in ODS steels", PhD thesis supervised by M.-F. Barthe, Orléans, Université d'Orléans, 2018, https://tel.archives-ouvertes.fr/tel-02395001.
[32] A. van Veen *et al.*, AIP Conference Proceedings **218**, 171 (1990).
[33] A. Vehanen *et al.*, Phys. Rev. B **29**, 2371 (1984).
[34] P.J. Schultz and K.G. Lynn, Rev. Mod. Phys. **60**, 701 (1988).
[35] Y. Xu *et al.*, Modern Physics Letters B **17**, 147 (2003).
[36] D.R. Mason *et al.*, J. Phys.: Condens. Matter. **26**, 375701 (2014).
[37] S.L. Dudarev, "DPA definition and estimates", https://www-amdis.iaea.org/CRP/IrradiatedTungsten/RCM2/RCM2Presentation-DudarevDPA-2015-09-10.pdf).
[38] P.E. Lhuillier *et al.*, Physica Status Solidi C **6**, 2329 (2009).
[39] A. Debelle, M.-F. Barthe, and T. Sauvage, Journal of Nuclear Materials **376**, 216 (2008).
[40] M. Sidibe, "Study of the behaviour of tungsten under irradiation: application to fusion reactors", PhD thesis supervised by M.-F. Barthe, Orléans, Université d'Orléans, 2014, https://tel.archives-ouvertes.fr/tel-01068634.
[41] X. Yi *et al.*, Acta Materialia **112**, 105 (2016).
[42] P.M. Derlet and S.L. Dudarev, Physical Review Materials **4**, 023605 (2020).
[43] M.-C. Marinica *et al.*, J. Phys.: Condens. Matter. **25**, 395502 (2013).
[44] D.R. Mason, D. Nguyen-Manh, and C.S. Becquart, J. Phys.: Condens. Matter **29**, 505501 (2017).
[45] M.W. Thompson, Philosophical Magazine **5**, 278 (1960).
[46] J. Heikinheimo *et al.*, APL Mater. **7**, 021103 (2019)
[47] F. Ferroni *et al.*, Acta Materialia **90**, 380 (2015).